

Detection of Trace Impurity Gradients in Noble Metals by the Photothermoelectric Effect

Charlotte I. Evans,¹ Lucia T. Gan,¹ Rui Yang, Mahdihyeh Abbasi, Xifan Wang, Rachel Traylor, Jonathan A. Fan,^{*} and Douglas Natelson^{*}



Cite This: *J. Phys. Chem. C* 2021, 125, 17509–17517



Read Online

ACCESS |



Metrics & More

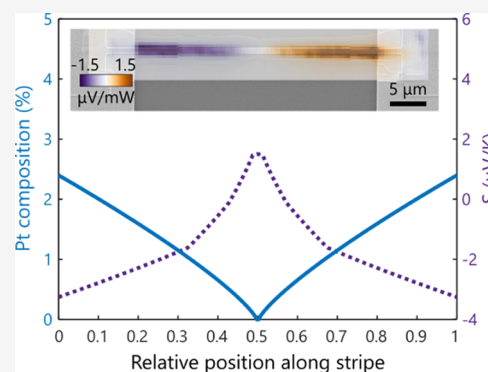


Article Recommendations



Supporting Information

ABSTRACT: Trace impurity concentrations in noble metals can have profound effects on chemical and physical properties, yet detecting these impurity concentrations remains a challenge using typical spectroscopic characterization tools and specialized techniques such as secondary ion mass spectrometry. In this work, we demonstrate that the photothermoelectric effect can be leveraged to detect low-concentration platinum gradients in wire-shaped gold nanostructures with high sensitivity. The photothermoelectric voltage measurements show significant contributions from platinum impurities to the bulk Seebeck coefficient of gold at length scales that agree with theoretical platinum diffusion lengths. Using finite element modeling, the Seebeck distribution is calculated for the gold–platinum system, showing that even a 0.01% variation in platinum concentration along a 1 μm length of gold wire can contribute significantly to the local Seebeck coefficient. These measurements indicate that the photothermoelectric effect can be a highly sensitive tool for detecting low-level impurity concentrations in host metals in a wire geometry.



INTRODUCTION

Trace impurities within a host metal can have profound effects on chemical and physical properties.^{1,2} Of particular interest is platinum in gold down to single platinum atoms, which can actively promote important electrocatalytic reactions, such as oxygen reduction and hydrogen evolution reactions that play a principle role in fueling clean energy sources.^{3–5} Doping gold clusters with platinum can lead to increased hydrogen absorption activity that is different from that of both gold and platinum.⁶ On the other hand, the presence of platinum impurities in gold catalysts can be detrimental to selective carbon dioxide reduction activity as they enhance the competing hydrogen evolution reaction.⁷

In metal systems such as these, it remains a challenge to quantify the presence of sub-1% concentrations of trace impurities. Typical metrology and characterization tools, including energy-dispersive X-ray spectroscopy, X-ray photoelectron spectroscopy, wavelength-dispersive spectroscopy, and Auger electron spectroscopy, are restricted by minimum elemental detection limits around 1%.⁸ Higher sensitivity techniques, including X-ray absorption spectroscopy and secondary ion mass spectrometry (SIMS), require specialized equipment or synchrotron sources. SIMS is a common doping measurement technique that generally offers the highest sensitivity for most elements and has been used to great success for identifying light organic species.⁹ However, it may not have the sensitivity required to detect very low

concentrations of high atomic mass metals that lack an abundance of stable isotopes, especially when embedded in a matrix composed of a metal with similar mass (e.g., low concentration of platinum in gold).

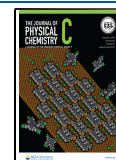
Here, we show that the photothermoelectric (PTE) effect can be leveraged to detect variations in the Seebeck coefficient along a wire-shaped nanoscale device, which serves as a proxy for measuring the platinum composition. The Seebeck coefficient, S , of a metal largely depends on the band structure and electron scattering in the material and, therefore, can serve as a sensitive probe of inhomogeneous distributions of impurities in nanoscale structures.

In noble metals such as gold, the positive sign of S primarily stems from the energy dependence of the electron mean free path.^{10,11} Altering the electronic scattering properties of a noble metal by introducing impurity atoms can result in large changes in S . The effects of impurities such as Mn, Pd, and Pt on S of bulk gold and the other noble metals have been studied for decades.^{12–16} At room temperature, alloying gold with even 0.5% platinum has been demonstrated to change the sign of S

Received: June 4, 2021

Revised: July 20, 2021

Published: August 2, 2021



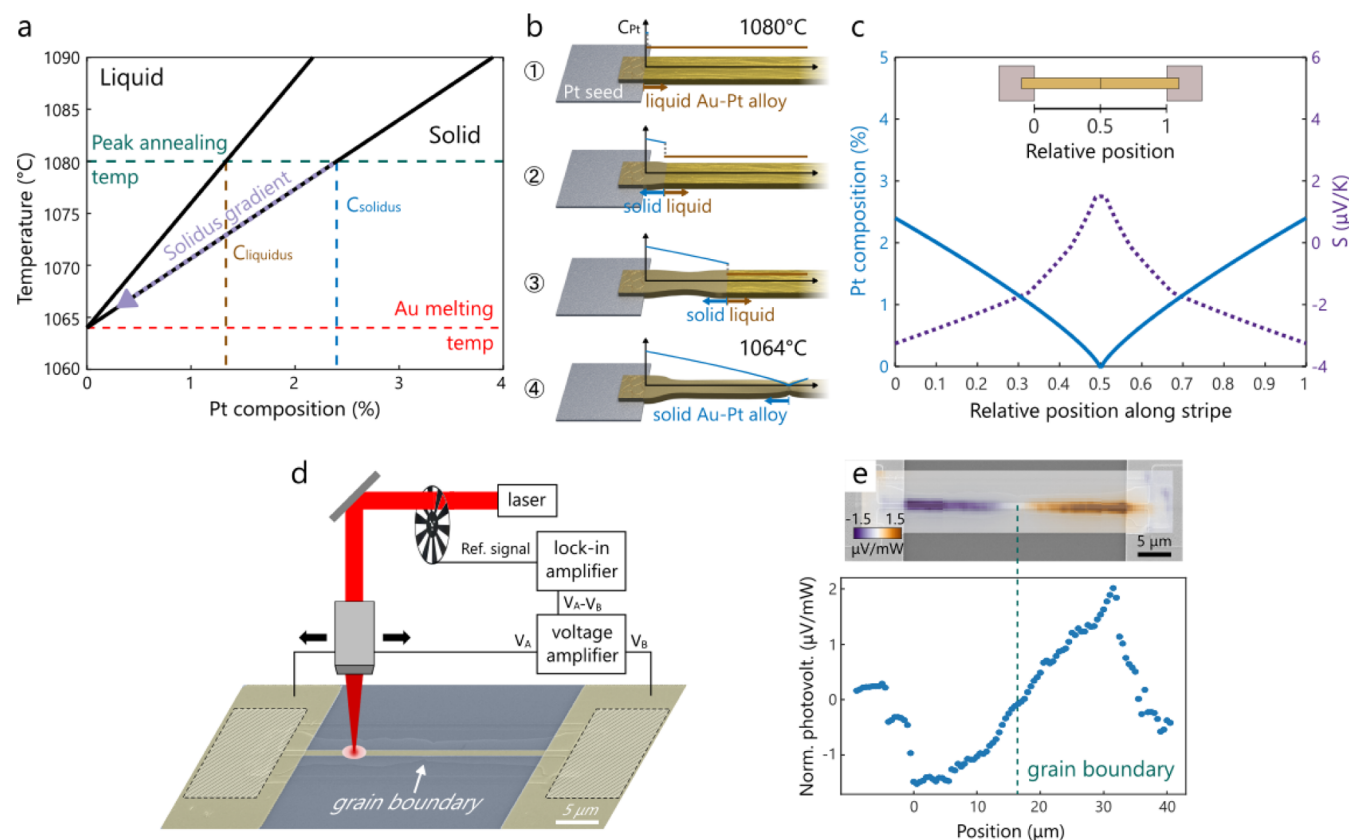


Figure 1. (a) Gold–platinum binary phase diagram at low platinum concentrations. The liquidus and solidus concentrations at the peak annealing temperature are marked. (b) Gold–platinum solidification process, shown for half of a bicrystal. (1) At 1080 °C, the gold stripe liquefies and platinum uniformly mixes in the gold until the liquidus concentration of 1.3% is reached, after which the alloy crystallizes with the solidus concentration of 2.4%. (2) As the system cools, the alloy solidifies with a concentration following the solidus line. (3) Platinum solute continues to redistribute from the liquid to the solid and the solid–liquid interface advances. (4) At 1064 °C, the gold stripe fully solidifies with a platinum concentration gradient. (c) Theoretical platinum concentration profile in bicrystal gold wires overlaid with the corresponding change in the Seebeck coefficient. (d) Schematic of the experimental setup. A raster-scanned laser serves as a heat source that generates an open-circuit PTE voltage across a gold wire measured via lock-in techniques. The platinum seed locations are shaded. (e) Photovoltage as a function of position is mapped by raster scanning the laser, allowing inference of the position-dependent Seebeck coefficient. The voltage uncertainty from the measurement is 0.2% for the individual data points in the color map. The data points in the line cut have a statistical error of 8% due to averaging the signal that spans across the whole width of the wire, which includes the sample edges.

from positive to negative, as the foreign atoms increase the energy-dependent scattering cross section, which affects both the phononic and electronic contributions to S .^{12,16} Further increasing the platinum concentration in the alloy results in an increasingly negative S . Thus, the relative impurity concentration can be revealed by measuring the change in S of this noble metal. Previous studies focused primarily on uniformly alloyed impurities in bulk noble metals without regard to the specifics of the impurity distribution. Due to the sensitivity of gold's S on the presence of platinum, probing the spatially dependent S allows us to exploit the PTE effect to probe the platinum distribution in gold nanostructures.

In this work, we map local changes in S along the lengths of single- and bicrystalline gold wires that possess low-concentration platinum gradients. We track the variation in S using a focused, raster-scanned laser as a heating source and measuring the steady-state, open-circuit photovoltage as a function of laser position. While the presence of platinum detected in the wires using the PTE technique is corroborated by NanoSIMS analysis, we find that NanoSIMS measurements lack the sensitivity to accurately and quantitatively reflect the entire platinum concentration profile when embedded in gold. Comparisons of gold bicrystals of varying lengths from

different fabrication runs with distinct platinum gradients demonstrate that the PTE voltage measurements are sensitive enough to detect minute differences in sub-1% platinum distributions. Through finite element modeling, the spatially varying S is inferred and demonstrates that a variation of platinum concentration as little as 0.01% per μm can have readily detectable effects on the PTE signal. The presence of platinum impurities has a much greater effect on the PTE voltage magnitude than other crystal disorder effects in the wire such as strain. These results indicate that PTE voltages can serve as a sensitive probe of inhomogeneous platinum impurities distributed in gold, which otherwise cannot be detected using conventional compositional analysis techniques.

METHODS

Fabrication. Samples were grown according to previously published methods.^{17,18} 300 nm of thermal SiO_2 was grown on Si substrates, followed by 30 nm of electron beam-evaporated Pt with a 2 nm Ti adhesion layer. $10\ \mu\text{m}$ by $10\ \mu\text{m}$ seeds were defined using photolithography followed by metal liftoff. Then, 100 nm of electron beam-evaporated Au was deposited and defined into $4\ \mu\text{m}$ wide stripes with varying lengths from 40 to

400 μm using photolithography and liftoff. The metal structures were encapsulated in 3 μm of LPCVD SiO_2 , annealed to 1080 $^\circ\text{C}$ at a rate of 15 $^\circ\text{C}/\text{s}$ in a rapid thermal annealer, and cooled to room temperature at a similar rate. Stripes seeded at a single end produced Au single crystals, while stripes seeded at both ends produced bicrystals with a single grain boundary at their centers. After the annealing cycle, the LPCVD SiO_2 crucible was removed through a dry plasma etch. Au wires approximately 600 nm in width were defined in the single-crystal and bicrystal stripes using electron beam lithography and argon ion beam milling. 150 nm of electron beam-evaporated Au with a 2 nm Ti adhesion layer was defined into electrical contact pads through photolithography and liftoff. The contact pads were deposited approximately 20–60 μm apart. Finally, the chip was mounted on a leadless chip carrier and wire-bonded for photovoltage measurements.

Experiment. A home-built Raman microscope with a piezo-controlled lens to control the position of a focused, linearly polarized 785 nm CW diode laser with a maximum intensity of 700 mW/cm^2 with a full width half-maximum (fwhm) diameter of 1.8 μm was used to optically heat the single- and bicrystal devices described above. This limits the spatial resolution of the PTE measurement, as discussed in detail in Supporting Information in refs 19 and 20. The laser has a positional stability on the sample of ~ 5 nm. The devices were kept at room temperature in a closed cycle cryostat (Montana Instruments) under high vacuum. The polarization of the laser was controlled using a half-wave plate. The polarization was kept at 90° , perpendicular to the length of the wire. The laser intensity was controlled using an ND filter and was modulated to a square wave with a frequency of 287 ± 0.1 Hz using a mechanical chopper, which served as the reference for the SR7270 DSP lock-in amplifier. The period of the laser intensity modulation is much longer than the thermalization time scale,²¹ so the PTE voltage data are recorded in the steady state. The integrated, steady-state open-circuit photovoltage of the device as a function of laser position was detected by measuring the potential difference between the two ends of the device which was amplified using the SR560 low noise precurrent amplifier as the input of the lock-in amplifier. A total of 55 single crystals and 40 bicrystals were measured. The devices described in this work were of typical device behavior.

NanoSIMS analysis was performed using a Cameca NanoSIMS 50L with the spot size specified by the $D_1 = 2$ aperture. The spatial resolution of the NanoSIMS maps is 200 nm. The primary ion current was 12 pA, and the ion counts were integrated over 25 ms. The NanoSIMS data were analyzed using the OpenMIMS plugin for ImageJ.

Simulations. For additional details of the finite element modeling and PTE/Seebeck distribution analysis, see Supporting Information.

RESULTS AND DISCUSSION

The devices studied in this work are single-crystal¹⁷ and bicrystal¹⁸ gold wires that are prepared on a thermally oxidized Si substrate to provide thermal and electrical isolation and fabricated using the metal-on-insulator rapid melt growth technique. In this growth process, a polycrystalline gold stripe and polycrystalline platinum seed are annealed at a high temperature above gold's melting point of 1064 $^\circ\text{C}$. At the peak annealing temperature of 1080 $^\circ\text{C}$, platinum quickly diffuses from the solid seed region into the encapsulated liquid

gold until the platinum concentration reaches the liquidus concentration of about 1.3%, indicated on the binary phase diagram in Figure 1a. At this point, the gold–platinum alloy begins to crystallize and once fully solidified, the platinum concentration reaches the solidus concentration of about 2.4%. As the structure cools from melt, the platinum concentration decreases away from the seed following the solidus concentration, resulting in a platinum concentration gradient that controls directional solidification (Figure 1b). Gold bicrystal wires, possessing a single grain boundary, are seeded symmetrically by two platinum seeds, one at each end of the wire. The platinum gradient plays a key role in single-crystal growth, and in bicrystals, it forces the grain boundary to form at the center of each wire regardless of the crystal orientation of adjacent grains. These 100 nm-thick devices are then lithographically defined and etched to a uniform width of approximately 600 nm. Gold pads for wire bonding are deposited over both ends for open-circuit photovoltage measurements.

The theoretical platinum distribution produced by the directional growth process in gold bicrystal wires can be predicted using the Scheil–Gulliver model for solidification.²² The model assumes the platinum mixes uniformly in liquid gold, which is most accurate if the diffusion length in the liquid phase is much greater than the length of the stripe, and no diffusion occurs in the solid phase. These requirements are moderately satisfied by bicrystals that have lengths less than 80 μm in length, which are studied in this article. The platinum profile within each grain of a bicrystal is modeled by solving the differential equation

$$(C_s - C_l)dx_s = (1 - x_s)(-dC_l) \quad (1)$$

The solidus and liquidus compositions, C_s and C_l , respectively, at the solid–liquid interface at local equilibrium are dictated by the phase diagram (Figure 1a). x_s represents the fraction of the metal that has solidified. Since the solidification process is necessarily symmetric for a bicrystal that is geometrically symmetric, the theoretical platinum concentration profile is shown by the blue line in Figure 1c and discussed at further length in Supporting Information. The corresponding changes to the local S can be approximated using interpolated literature values (Figure S2),¹³ shown by the purple dotted line in Figure 1c, and experimentally interrogated by measuring the open-circuit photovoltage as a function of position.

The integrated, steady-state, open-circuit PTE voltage of the device is measured between the two ends of a device using a focused laser as a heat source in a home-built Raman microscope depicted in Figure 1d, similar to previous works.^{19,20,23–25} The photovoltage measurements are acquired using a linearly polarized 785 nm diode laser as the heat source focused via an optical objective to an fwhm of 1.8 μm onto the gold wires, which are placed in a cryostat under high vacuum at room temperature. The laser position is controlled using an optical lens and the intensity is modulated using a mechanical chopper at a frequency of 287 Hz, used as a reference for the lock-in amplifier, which measures the voltage difference across the wire.

The width of the wires is much smaller than the laser fwhm, so the system can be treated as effectively one-dimensional in x . The focused laser heats the wire at a point along its length, l , which produces a temperature gradient, ∇T , and generates an

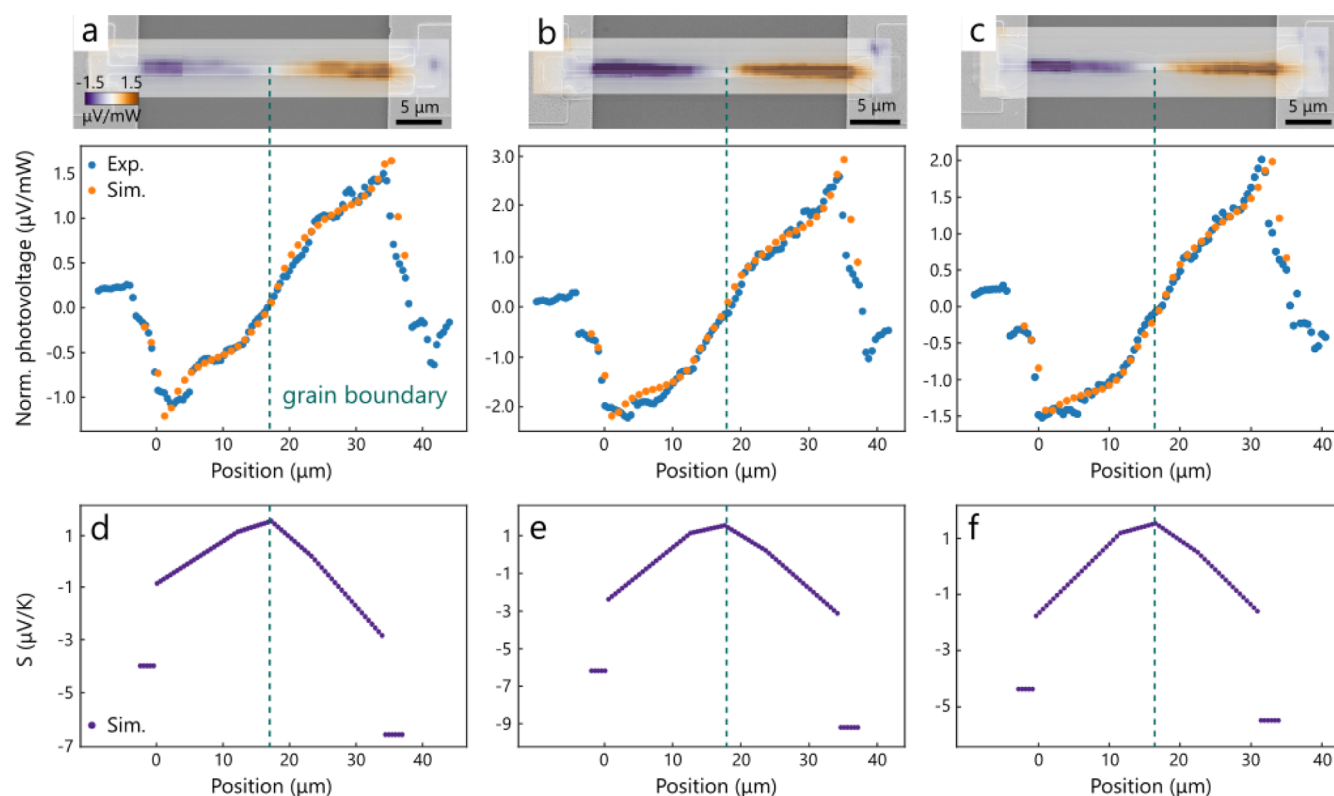


Figure 2. (a–c) PTE voltage maps of 40 μm -long bicrystal wires are overlaid on the corresponding SEM images. The voltages are normalized to the incident laser power. The accompanying photovoltage scatter plots are averaged across the width of each wire, along with the simulated photovoltage response. The grain boundaries are demarcated by the dotted green lines where the photovoltage is near zero. The photovoltage signal is approximately linear and antisymmetric about each grain boundary. Blue points represent measured data, and orange points represent the simulated PTE voltage distribution from finite element modeling that result from the Seebeck coefficient distributions shown by the purple points in (d–f). As mentioned before, the voltage uncertainty from the PTE measurement is 0.2% for the individual data points in the color map. The data points in the line cut have a statistical error of 8% due to averaging the signal that spans across the whole width of the wire, which includes the sample edges.

open-circuit PTE voltage, V , across the wire that is proportional to the local S , given by

$$V(x) = \int_0^l S(x, T(x)) \nabla T(x) dx \quad (2)$$

The position-dependent $S(x)$ can therefore be mapped by raster scanning the laser along the length of a wire and measuring the PTE voltage as a function of position using lock-in detection (Figure 1e). Since the geometry of the wire is plasmonically nonresonant under 785 nm illumination and the substrate is at room temperature, heating from absorption is modest and thermal transport is comparatively efficient. The voltage measurements are linearly dependent on laser power²⁰ and, in this article, are normalized to an incident power of 15 mW. The polarization of the laser is oriented with the electric field perpendicular to the length of the wire.

The gold bicrystal wires measured in Figure 2 are 40 μm in length and manufactured on the same chip. The electrical contact pads are placed 30 μm apart symmetrically about each grain boundary, which are delineated by the dotted green lines. The two-dimensional (2D) photovoltage maps are overlaid on the scanning electron microscopy (SEM) images of the corresponding bicrystal devices. When the laser is incident on the grain boundary, which defines the device's geometric axis of symmetry, the PTE voltage is near zero. On either side of the grain boundary, the voltage is of opposite polarity and varies approximately linearly over 30 μm , over 15 times larger

than the focused laser spot fwhm. The largest signal magnitude occurs close to the electrodes approximately 15 μm on either side of the grain boundary. In contrast to measurements in platinum-free gold structures,²⁰ the grain boundary seems to define the location of a sign flip in photovoltage. The voltage uncertainty from the measurement is 0.2% for the individual data points within the 2D maps. Simulations suggest that a 1.8 μm fwhm focused beam diameter results in a temperature increase of ~ 2 K and should not appreciably heat the grain boundary at a distance greater than 10 μm around the boundary (Figure S7), which indicates that the maximum signal is neither set by the grain boundary itself nor the laser spot size.

The scatter plots in Figure 2 display the photovoltage averaged across the device width. Because these points represent the averaged signal across the entire width of the device which includes the milled edges, which can result in a plasmonically resonant response due to roughness, the statistical error of each scatter point is 8%, which is larger than the individual point uncertainty of 0.2%. The observed PTE voltage signals can be simulated via finite element modeling using a spatial distribution of S , which are shown in Figure 2d–f. The finite element modeling simulations were performed using COMSOL Multiphysics Joule Heating Physics and are discussed in greater detail in Supporting Information. Based on the platinum concentration model in Figure 1c, we assume that $S = 1.5 \mu\text{V/K}$ at the grain boundary,

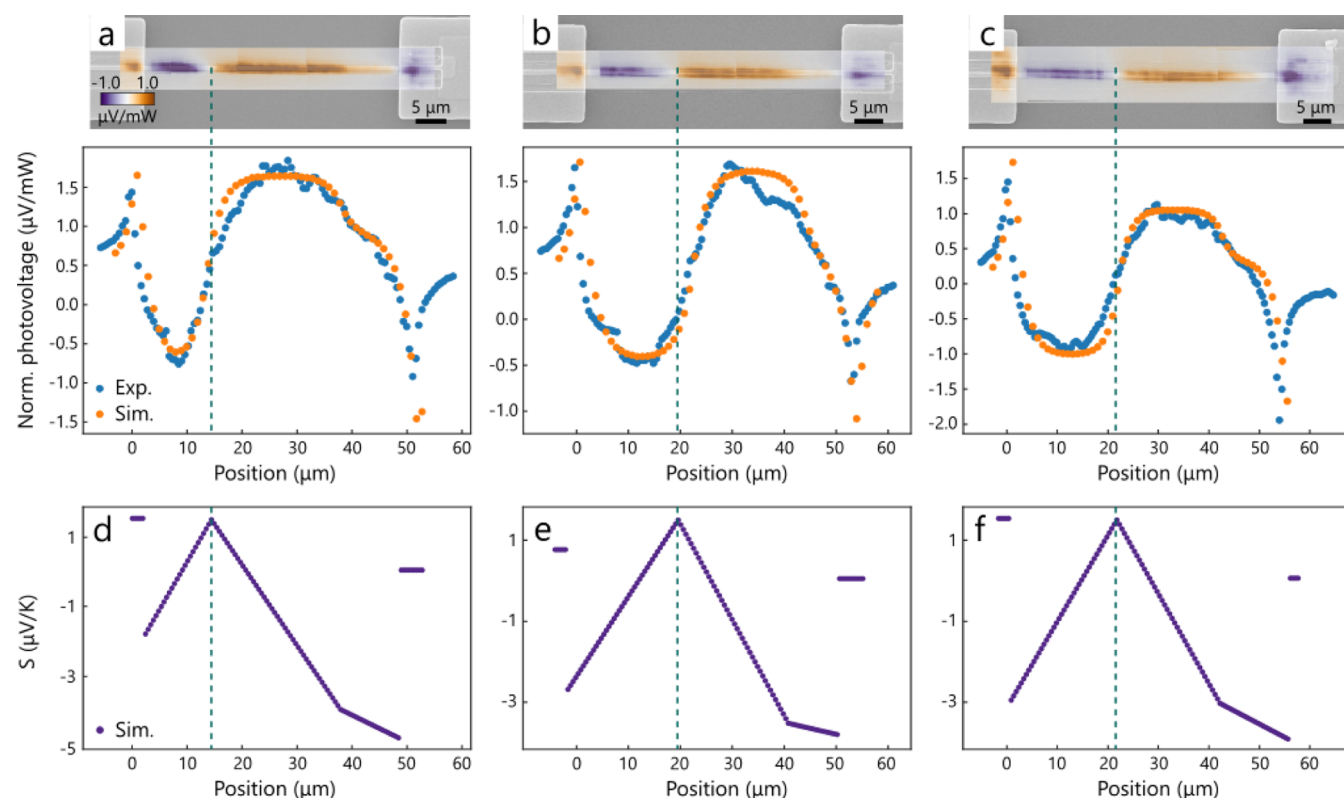


Figure 3. (a–c) PTE voltage maps of 80 μm -long bicrystal wires are overlaid on the corresponding SEM images. In the 10–20 μm region around the grain boundary, the photovoltage signal is approximately linear and antisymmetric with a slightly steeper slope than the measurements from Figure 2. The devices are from a separate fabrication run and possess a different platinum concentration profile from the previous figure. Blue points represent measured data, and orange points represent the simulated PTE voltage distribution from finite element modeling that result from the Seebeck coefficient distributions shown by the purple points in (d–f). As mentioned before, the voltage uncertainty from the measurement is 0.2% for the individual data points in the color map. The data points in the line cuts have a statistical error of 8% due to averaging the signal that spans across the whole width of the wire, which includes the sample edges.

equal to that of pure gold. A gradient of S that varies approximately linearly at a rate of $0.22 \mu\text{V/K}$ per μm can reproduce the voltages observed in the experiment, which matches well with the predicted S distribution in Figure 1c. Although the absolute value or spatial distribution of S cannot be obtained via finite element modeling alone, these simulations indicate that a relatively simple spatial variation of S can result in the observed PTE voltages along the length of the wires.

A set of gold bicrystal wires that are 80 μm in length are displayed in Figure 3. These devices were taken from another chip that was manufactured in a separate fabrication run from those in Figure 2. The electrical contact pads are placed roughly 40–50 μm apart but are instead positioned asymmetrically about each grain boundary. The PTE response of these wires appear distinct from those in Figure 2, which signify that these wires possess a qualitatively different distribution of platinum in gold. Heating the grain boundary results in a near-zero PTE voltage with opposite polarity voltage on either side of the boundary. In these longer devices, the maximum voltage magnitudes arise about 10 μm from the grain boundary and slowly decreases further from the boundary before changing polarity at the electrical contacts. In the 10–20 μm region around the boundary, the voltage varies approximately linearly with a slightly larger slope than the measurements from Figure 2. The photovoltage profiles remain antisymmetric relative to the grain boundary despite the asymmetric placement of the contact pads. The overall

magnitude of the PTE voltage signals is comparable between both sets of devices. Assuming again that $S = 1.5 \mu\text{V/K}$ at the grain boundary, finite element modeling suggests that the measured PTE voltage signals can be observed by varying S approximately linearly at a rate of $0.22 \mu\text{V/K}$ per μm . Since the Scheil–Gulliver model is only dependent on the relative position, we expect that S would vary at half this rate because the wires are double the length.

From the spatial distributions of S in both sets of devices inferred through finite element modeling, shown in Figures 2d–f and 3d–f, the platinum concentration can be estimated. The distribution of S that resulted in the magnitude in PTE voltages observed in the experiment varied by about $0.2 \mu\text{V/K}$ over 1 μm . Previous experiments have shown that alloying gold with increasing platinum concentrations from 0.11 to 0.5% can change S by approximately $1.6 \mu\text{V/K}$.^{13,14} Based on these literature values, our simulations suggest that variations in a platinum concentration of $\sim 0.01\%$ per μm have detectable impact on S and can lead to the observed photovoltage magnitudes. Although we cannot obtain the absolute S through simulations, we can use the simulated S values to estimate the potential platinum concentration gradient in the structures using literature values (Figure S1).

We see that the PTE response from wire to wire is very similar for both Figures 2 and 3, but distinct from chip to chip. We suggest that the contrast in PTE response between the 40 and 80 μm bicrystals is attributed to the difference in wire length and subtle fabrication variability. First, the assumptions

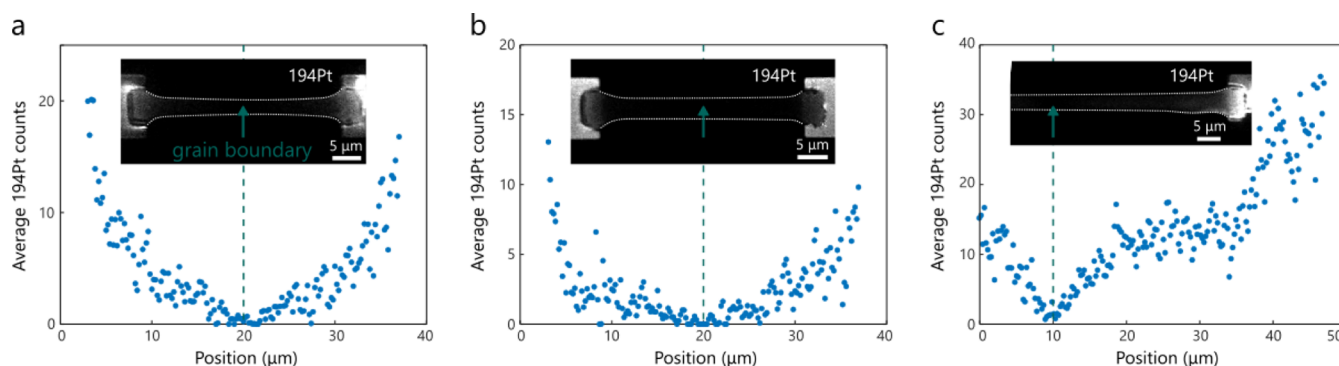


Figure 4. (a) NanoSIMS compositional analysis of a 40 μm -long bicrystal. The Pt-194 secondary ion counts are averaged across the width of each wire, which reveals a symmetric platinum gradient. The statistical uncertainty in the Pt-194 signal is evident from the spread in the data points. (b) NanoSIMS compositional analysis of a 40 μm -long bicrystal from a separate fabrication run. The plot reveals a symmetric platinum gradient across the wire that is distinct from that in (a). (c) NanoSIMS compositional analysis of an 80 μm -long bicrystal corresponding to the region measured in Figure 3.

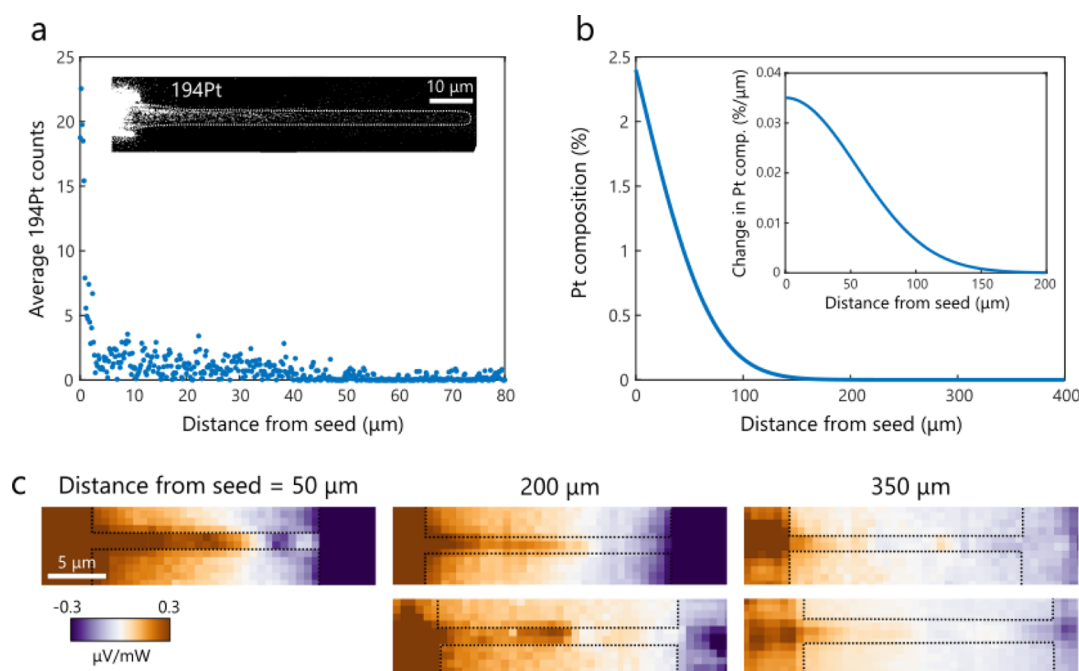


Figure 5. (a) NanoSIMS compositional analysis of an 80 μm -long single-crystalline structure. The signal reaches the detection limit of 1 count around 40 μm away from the seed. (b) Theoretical platinum concentration profile in a long single-crystal gold wire. (c) PTE voltage maps of 400 μm -long single-crystal wires at increasing distances from the platinum seed with contact pads placed 20 μm apart. Distances between 50 and 350 μm from the seed show a significant difference in magnitude and spatial variation. Dashed lines mark the position of the wires and contact pads.

made in computing the platinum diffusion profile in Figure 1c are more strongly satisfied for shorter bicrystals. The diffusion coefficient of similar solutes in other liquid fcc metal systems is on the order of $10^{-9} \text{ m}^2/\text{s}$, which translates to a diffusion length on the order of 40 μm for an annealing time of 1 s. Thus, the concentration gradient is less accurately predicted for the 80 μm wires, in which the diffusion length is comparable to the grain length. Second, any fabrication variability, such as the maximum annealing temperature, will modify the diffusion behavior and resultant platinum distribution. The structures are heated in a rapid thermal annealer system, which lacks precise control at high temperatures. As seen in the phase diagram, changing the peak annealing temperature by a few degrees can significantly change the initial platinum composition. To demonstrate this effect, we estimate the platinum concentration from the

simulated S profiles using literature values and fit a Scheil–Gulliver profile to the data (Figure S2), which shows that even a 6 $^\circ\text{C}$ variance from the desired maximum annealing temperature could account for the difference in PTE response. The differences from chip to chip between bicrystals of varying lengths were consistently observed across 40 unique bicrystal devices.

Nanoscale SIMS (NanoSIMS) was employed to probe the qualitative differences in the platinum profile between the gold wires. NanoSIMS is a destructive characterization technique in which negative secondary ions are ejected from a sample using a focused cesium ion beam and collected in a mass spectrometer. By sputtering the gold wire with a focused cesium ion beam, we can qualitatively measure the elemental composition of the surface layers of the gold stripe. Figure 4a,b shows NanoSIMS analysis of a representative bicrystal from

each chip. The wire in Figure 4a is representative of the devices measured in Figure 2, and Figure 4b shows representative of the devices measured in Figure 3. Both bicrystals are 40 μm long to illustrate the differences in platinum diffusion resulting from fabrication variability but qualitatively exhibit the expected platinum concentration profile. Figure 4c shows NanoSIMS analysis of part of an 80 μm bicrystal corresponding to a similar region measured using the scanning laser probe. As expected, we see a deviation from the theoretical profile due to the longer length. The platinum appears to decrease exponentially near the seeds but exhibits Scheil–Gulliver behavior near the grain boundary. In the plots, the Pt-194 secondary ion counts are averaged across the width of the wires. The statistical uncertainty in the Pt-194 signal is evident from the spread in the data points. The NanoSIMS profile confirms that the grain boundary demarcates not only the structural axis of symmetry but also the symmetry axis for the platinum gradient. The grain boundary locations can be clearly observed by characteristic grooves in the corresponding secondary electron image acquired simultaneously using the NanoSIMS secondary electron detector (Figure S3). While all wires exhibit a monotonically decreasing platinum concentration at increasing distances from the seed similar in shape to the predicted profile in Figure 1c, the platinum profiles in the wires are qualitatively different.

Typically, NanoSIMS can offer ppm-level detection, but the gold–platinum system in particular poses many challenges to achieving high sensitivities. First, accurate calibration standards are required in order to achieve reliable quantification of concentrations, which are difficult to produce at low concentrations. The second challenge relates to isotopic abundance. Gold possesses a single stable isotope Au-197 and ejects a large number of secondary ions under the focused beam (Figure S4). On the other hand, platinum has five stable isotopes ranging from 192 to 198 amu, none of which are produced abundantly, which limits the ion yield. Furthermore, the matrix effect inherently causes the presence of gold to change the platinum ion yield.²⁶ Third, there are physical limitations on how closely spaced the detectors can be positioned in the mass spectrometer, which restrict the mass resolution of higher atomic number species. The minimum mass interval between adjacent detectors is $M_{\text{max}}/58 \approx 3.4$ amu.²⁷ Therefore, we cannot simultaneously collect all isotopes of platinum to improve secondary ion yield and cannot simultaneously collect secondary ions from elements with similar atomic mass. In this study, we choose to measure the prevalence of Pt-194 secondary ions due to its abundance and its mass being the most distinct from that of gold. However, parallel detection of Au-197 and Pt-194 with a mass interval of 3 amu is already impeded, which lowers the detection efficiency and measurement accuracy.

On much longer length scales, we also show that the diffusion profile of platinum takes on a different behavior. Figure 5a shows the NanoSIMS data from an 80 μm -long single-crystalline wire that does not satisfy the requirements for the Scheil–Gulliver diffusion model previously presented. The platinum concentration decreases exponentially as the distance from the platinum seed increases. Additionally, we observe that the detection limit of 1 ion count is quickly reached as close as 40 μm away from the seed. This prevents us from deriving an accurate and quantitative picture of the platinum concentration profile in wires much longer than the diffusion length.

In order to corroborate scanning PTE measurements, we modeled the expected platinum diffusion length in liquid gold. The atomic diffusivity of the platinum metal in gold's solid phase as a function of temperature is well-documented in the literature,²⁸ but there remains an absence of studies of platinum's temperature-dependent diffusivity in liquid gold at temperatures above gold's melting point. We use a modified Andrade equation²⁹ to calculate the temperature-dependent viscosity of liquid gold to be 5.6 mPa·s at 1080 °C. This value is reasonable compared to studies of gold evaluated at 1064 °C with viscosities of 5³⁰ and 5.16 mPa·s.³¹ Since the platinum solute is comparable in size to the gold solvent atoms, we use a modified Sutherland diffusion equation to relate the viscosity to platinum impurity diffusivity in liquid gold,³² which we calculate to be $1.5 \times 10^{-9} \text{ m}^2/\text{s}$, which is on the same order of magnitude as impurity diffusion coefficients in other liquid metal systems.³² The calculations are discussed in detail in Supporting Information. Using this value, the platinum concentration in a 400 μm -long gold wire can be modeled using the solution to Fick's second law for a very long wire with an infinite platinum source (Figure 5b), where the initial concentration is dictated by the solidus composition at the peak annealing temperature. We assume that the bulk of the platinum diffuses, while the gold is in its liquid phase, which is a valid assumption because the atomic diffusivity of platinum in gold's solid form is approximately 5 orders of magnitude lower than in liquid.³³ The platinum gradient approaches zero around 200 μm away from the seed. In addition, the change in platinum concentration (Figure 5b inset) aligns well with the prediction that changes in concentration of 0.01% per 1 μm are readily detectable using the PTE effect.

To validate this model, we measured a series of 400 μm -long single-crystalline wires in 20 μm segments at distances between 50 and 350 μm away from the seeds (Figure 5c). As the distance from the platinum seed increases, the photovoltage magnitudes decrease, while the spatial variation occurs on shorter length scales. Although the platinum concentration in these wires is sufficiently low such that detection via NanoSIMS is challenging, the scanning laser measurements still appear sensitive to the presence of the platinum gradient. Many distinct single-crystalline devices were measured with contact pads placed 20 μm apart at different positions along the lengths of the single-crystal wires and displayed a similar behavior (Figure S5). In general, the devices measured close to the platinum seed have slowly varying photovoltage signals with larger magnitudes on the order of 1 $\mu\text{V}/\text{mW}$. At around 200 μm , micron-scale spatial variations begin to arise that are 2 orders of magnitude lower in signal on the order of 0.01 $\mu\text{V}/\text{mW}$. The larger photovoltage magnitude detected for the devices closest to the platinum seeds is likely a result of the steeper platinum gradient that produces larger changes to gold's S . The length scale and magnitudes of the slowly varying signal also suggest that the diffusion length of platinum in liquid gold is close to 200 μm .

The overall magnitude of the photovoltages measured close to the platinum seed is on the order of 1 $\mu\text{V}/\text{mW}$, which is 100 \times larger than the magnitudes observed in the platinum-free devices discussed in our previous work.²⁰ In contrast with our previous work, these changes in S are too substantial and occur on length scales too large to arise only from crystallographic defects and strain associated with misorientation. Tensile measurements from the literature conducted on polycrystalline gold imply that 100% strain would change the bulk S by 6.3

$\mu\text{V/K}$.³⁴ In order to account for the magnitude of change in S shown in this work, our sample would be required to undergo over 50% strain, which is nonphysical. The inferred mechanism driving the large photovoltage variations in this article is instead dominated by the presence of the low-concentration platinum gradient that overwhelms and obscures the signal correlated to crystal deformation. We see in Figure 5c that at distances greater than 200 μm from the platinum seed, lower signal micron-scale variations on the order of 0.01 $\mu\text{V/mW}$ arise that are connected to crystallographic defects and strain associated with misorientation within the single crystals. These variations only become evident once the platinum gradient approaches zero.

CONCLUSIONS

We find that scanning PTE measurements are effective at detecting trace platinum impurities in gold with concentrations less than 1% when using traditional characterization methods is impractical. We show that even with highly specialized NanoSIMS analysis, detecting platinum impurities in gold nanostructures is difficult compared to the PTE effect, which serves as a highly sensitive probe to variations in the Seebeck coefficient in a noble metal. Open-circuit photovoltage maps of bicrystal gold devices with varying platinum gradients exhibit distinct voltage profiles that reveal qualitatively different platinum distributions. The length scales of detected platinum in single-crystal devices closely match that of theory. Finite element modeling demonstrates that variations in platinum concentration as little as 0.01% along 1 μm can have large effects in the Seebeck coefficient in these structures. The PTE effect is therefore a powerful tool to detect impurities in noble metal nanostructures that can affect the electronic transport properties of the device.

ASSOCIATED CONTENT

Supporting Information

The Supporting Information is available free of charge at <https://pubs.acs.org/doi/10.1021/acs.jpcc.1c04927>.

Quantitative discussion of diffusion models; further details of the NanoSIMS analysis; and greater description of the finite element modeling and PTE/Seebeck/thermal distribution modeling (PDF)

AUTHOR INFORMATION

Corresponding Authors

Jonathan A. Fan – Department of Electrical Engineering, Stanford University, Stanford, California 94305, United States; orcid.org/0000-0001-9816-9979; Email: jonfan@stanford.edu

Douglas Natelson – Department of Physics and Astronomy, Rice University, Houston, Texas 77005, United States; orcid.org/0000-0003-2370-9859; Email: natelson@rice.edu

Authors

Charlotte I. Evans – Department of Physics and Astronomy, Rice University, Houston, Texas 77005, United States

Lucia T. Gan – Department of Electrical Engineering, Stanford University, Stanford, California 94305, United States

Rui Yang – Department of Electrical Engineering, Stanford University, Stanford, California 94305, United States; Present Address: University of Michigan-Shanghai Jiao

Tong University Joint Institute, Shanghai Jiao Tong University, Shanghai 200240, China

Mahdiyeh Abbasi – Department of Electrical and Computer Engineering, Rice University, Houston, Texas 77005, United States

Xifan Wang – Department of Materials Science and NanoEngineering, Rice University, Houston, Texas 77005, United States

Rachel Traylor – Department of Electrical Engineering, Stanford University, Stanford, California 94305, United States

Complete contact information is available at:

<https://pubs.acs.org/doi/10.1021/acs.jpcc.1c04927>

Author Contributions

[†]C.I.E. and L.T.G. contributed equally to this work.

Notes

The authors declare no competing financial interest.

ACKNOWLEDGMENTS

The authors thank William D. Nix for discussions on platinum diffusion modeling. D.N. and C.I.E. acknowledge support from Robert A. Welch Foundation grant C-1636. D.N., M.A., and X.W. acknowledge support from the National Science Foundation award no. ECCS-1704625. J.A.F., L.T.G., R.Y., and R.T. acknowledge support from the NSF under award 1804224, the Air Force Office of Scientific Research Multidisciplinary University Research Initiative under Award FA9550-16-1-0031, and the Packard Fellowship Foundation. R.Y. acknowledges support from Shanghai Sailing Program under award 19YF1424900 and from University of Michigan–Shanghai Jiao Tong University Joint Institute in Shanghai Jiao Tong University. Part of this work was performed at the Stanford Nanofabrication Facility and the Stanford Nano Shared Facilities, supported by the NSF under award ECCS-1542152.

REFERENCES

- (1) Giannakakis, G.; Flytzani-Stephanopoulos, M.; Sykes, E. C. H. Single-atom alloys as a reductionist approach to the rational design of heterogeneous catalysts. *Acc. Chem. Res.* **2018**, *52*, 237–247.
- (2) Greiner, M. T.; Jones, T. E.; Beeg, S.; Zwiener, L.; Scherzer, M.; Girgsdies, F.; Piccinin, S.; Armbrüster, M.; Knop-Gericke, A.; Schlögl, R. Free-atom-like d states in single-atom alloy catalysts. *Nat. Chem.* **2018**, *10*, 1008–1015.
- (3) Greeley, J.; Stephens, I. E. L.; Bondarenko, A. S.; Johansson, T. P.; Hansen, H. A.; Jaramillo, T. F.; Rossmeisl, J.; Chorkendorff, I.; Nørskov, J. K. Alloys of platinum and early transition metals as oxygen reduction electrocatalysts. *Nat. Chem.* **2009**, *1*, 552–556.
- (4) Kye, J.; Shin, M.; Lim, B.; Jang, J.-W.; Oh, I.; Hwang, S. Platinum monolayer electrocatalyst on gold nanostructures on silicon for photoelectrochemical hydrogen evolution. *ACS Nano* **2013**, *7*, 6017–6023.
- (5) Cheng, N.; Stambula, S.; Wang, D.; Banis, M. N.; Liu, J.; Riese, A.; Xiao, B.; Li, R.; Sham, T.-K.; Liu, L.-M.; et al. Platinum single-atom and cluster catalysis of the hydrogen evolution reaction. *Nat. Commun.* **2016**, *7*, 13638.
- (6) Bus, E.; van Bokhoven, J. A. Hydrogen chemisorption on supported platinum, gold, and platinum-gold-alloy catalysts. *Phys. Chem. Chem. Phys.* **2007**, *9*, 2894–2902.
- (7) Peterson, A. A.; Nørskov, J. K. Activity descriptors for CO₂ electroreduction to methane on transition-metal catalysts. *J. Phys. Chem. Lett.* **2012**, *3*, 251–258.

- (8) Brandon, D.; Kaplan, W. D. *Microstructural Characterization of Materials*; John Wiley & Sons, 2013.
- (9) Zhai, Y.; DuChene, J. S.; Wang, Y.-C.; Qiu, J.; Johnston-Peck, A. C.; You, B.; Guo, W.; DiCiaccio, B.; Qian, K.; Zhao, E. W.; et al. Polyvinylpyrrolidone-induced anisotropic growth of gold nanoprisms in plasmon-driven synthesis. *Nat. Mater.* **2016**, *15*, 889–895.
- (10) Dreirach, O. The electrical resistivity and thermopower of solid noble metals. *J. Phys. F: Met. Phys.* **1973**, *3*, 577–584.
- (11) Robinson, J. E. Thermoelectric Power in the Nearly-Free-Electron Model. *Phys. Rev.* **1967**, *161*, 533–539.
- (12) Otter, F. A. Thermoelectric Power and Electrical Resistivity of Dilute Alloys of Mn, Pd, and Pt in Cu, Ag, and Au. *J. Appl. Phys.* **1956**, *27*, 197–200.
- (13) Huebener, R. P.; van Baarle, C. Thermoelectric Power of Annealed and Quenched Gold-Platinum Alloys. *Phys. Rev.* **1967**, *159*, 564–571.
- (14) Huebner, R. P.; Van Baarle, C. Thermoelectric power of annealed and quenched gold-platinum alloys at low temperatures. *Phys. Lett.* **1966**, *23*, 189–190.
- (15) Christenson, E. L. Effects of Transition Metal Solutes on the Thermoelectric Power of Copper and Gold. *J. Appl. Phys.* **1963**, *34*, 1485–1491.
- (16) Domenicali, C. A.; Otter, F. A. Thermoelectric Power and Electron Scattering in Metal Alloys. *Phys. Rev.* **1954**, *95*, 1134–1142.
- (17) Zhang, K.; Pitner, X. B.; Yang, R.; Nix, W. D.; Plummer, J. D.; Fan, J. A. Single-crystal metal growth on amorphous insulating substrates. *Proc. Natl. Acad. Sci. U.S.A.* **2018**, *115*, 685–689.
- (18) Gan, L. T.; Yang, R.; Traylor, R.; Cai, W.; Nix, W. D.; Fan, J. A. High-Throughput Growth of Microscale Gold Bicrystals for Single-Grain-Boundary Studies. *Adv. Mater.* **2019**, *31*, 1902189.
- (19) Zolotavin, P.; Evans, C. I.; Natelson, D. Substantial local variation of the Seebeck coefficient in gold nanowires. *Nanoscale* **2017**, *9*, 9160–9166.
- (20) Evans, C. I.; Yang, R.; Gan, L. T.; Abbasi, M.; Wang, X.; Traylor, R.; Fan, J. A.; Natelson, D. Thermoelectric response from grain boundaries and lattice distortions in crystalline gold devices. *Proc. Natl. Acad. Sci. U.S.A.* **2020**, *117*, 23350–23355.
- (21) Benner, D.; Boneberg, J.; Nürnberger, P.; Waitz, R.; Leiderer, P.; Scheer, E. Lateral and Temporal Dependence of the Transport through an Atomic Gold Contact under Light Irradiation: Signature of Propagating Surface Plasmon Polaritons. *Nano Lett.* **2014**, *14*, 5218–5223.
- (22) Scheil, E. Bemerkungen zur schichtkristallbildung. *Z. Metallkd.* **1942**, *34*, 70–72.
- (23) Zolotavin, P.; Evans, C.; Natelson, D. Photothermoelectric Effects and Large Photovoltages in Plasmonic Au Nanowires with Nanogaps. *J. Phys. Chem. Lett.* **2017**, *8*, 1739–1744.
- (24) Evans, C. I.; Natelson, D. Remote Excitation of Hot Electrons via Propagating Surface Plasmons. *J. Phys. Chem. C* **2019**, *123*, 10057–10064.
- (25) Abbasi, M.; Evans, C. I.; Chen, L.; Natelson, D. Single Metal Photodetectors Using Plasmonically-Active Asymmetric Gold Nanostructures. *ACS Nano* **2020**, *14*, 17535–17542.
- (26) Deline, V. R.; Katz, W.; Evans, C. A., Jr; Williams, P. Mechanism of the SIMS matrix effect. *Appl. Phys. Lett.* **1978**, *33*, 832–835.
- (27) Cameca, NanoSIMS 50L Users Guide. Cameca.
- (28) Mortlock, A. J.; Rowe, A. H.; Le Claire, A. D. The atomic diffusion of platinum in gold. *Phil. Mag. A J. Theor. Exp. Appl. Phys.* **1960**, *5*, 803–814.
- (29) Kaptay, G. A unified equation for the viscosity of pure liquid metals. *Z. Metallkd.* **2005**, *96*, 24–31.
- (30) Battezzati, L.; Greer, A. L. The viscosity of liquid metals and alloys. *Acta Metall.* **1989**, *37*, 1791–1802.
- (31) Egry, I.; Lohöfer, G.; Sauerland, S. Surface tension and viscosity of liquid metals. *J. Non-Cryst. Solids* **1993**, *156–158*, 830–832.
- (32) Chen, W.; Zhang, L.; Du, Y.; Huang, B. Viscosity and diffusivity in melts: from unary to multicomponent systems. *Phil. Mag.* **2014**, *94*, 1552–1577.
- (33) Mortlock, A. J.; Rowe, A. H.; Le Claire, A. D. The atomic diffusion of platinum in gold. *Phil. Mag.* **1960**, *5*, 803–814.
- (34) Amuzu, J. K. A. The effect of tensile stress on the thermoelectric E. M. F. in copper, gold, and silver. *Phys. Status Solidi A* **1981**, *63*, K7–K10.